Magnetically controlled topological braiding with Majorana corner states in second-order topological superconductors

Lizhou Liu,[1] Chengming Miao,[1] Hanzhao Tang [ORCID],[2] Ying-Tao Zhang [ORCID],[1,*] and Zhenhua Qiao [ORCID][3,4,5,†]

[1]*College of Physics, Hebei Normal University, Shijiazhuang 050024, China*

[2]*Department of Mathematics and Physics, Shijiazhuang Tiedao University, Shijiazhuang 050043, China*

[3]*International Centre for Quantum Design of Functional Materials, University of Scienceand Technology of China, Hefei, Anhui 230026, China*

[4]*CAS Key Laboratory of Strongly-Coupled Quantum Matter Physics, and Department of Physics, University of Science and Technology of China, Hefei, Anhui 230026, China*

[5]*Hefei National Laboratory, University of Science and Technology of China, Hefei 230088, China*

We theoretically investigate the electronic properties of finite-sized (e.g., triangular and diamond-shaped) Kane-Mele-type topological insulator nanoflakes on top of an *s*-wave superconductor. We find that the second-order topological superconductor can be generated when the magnetism is only applied on the system boundaries, which host two Majorana corner states located at the corners of two neighboring boundaries. By tuning the applied boundary magnetism, we observe that two isolated Majorana corner states can be adiabatically moved along the system boundaries. Furthermore, we show the possibility of performing topological quantum braiding of the Majorana corner states towards the far-reaching implications of quantum information and quantum computation.

I. INTRODUCTION

Topological quantum computation can eliminate decoherence by encoding logical information into anyons with non-Abelian statistics [1,2], and is considered to be the most effective approach to realize the fault-tolerant quantum computers. Majorana zero modes behave like Majorana fermions, each of which is an antiparticle of itself [3], and promise a platform for realizing a representation of non-Abelian braiding groups that enable topological quantum computation [4,5]. However, it remains controversial whether zero-energy signals are induced by Majorana zero modes in experimental systems such as unconventional superconductors [6,7], superconducting nanowires [8–13], ferromagnetic atomic chains [14], and two-dimensional superconducting vortices [15,16]. At any rate, it does not affect the exploration of Majorana zero modes' braiding design. Later, higher-order topological phases have also been proposed as novel topological phases of matter with nontrivial boundary states at multiple dimensionality. For example, Langbehn *et al.* proposed two-dimensional second-order topological superconductors to realize zero-dimensional Majorana zero modes [17]. By applying an external magnetic field [18–20], a first-order topological superconductor can be driven to be the second-order counterpart, where the localized Majorana zero modes appear at corners [21–24].

To realize the braiding operation of Majorana zero modes, the key procedure is the adiabatically time-dependent dynamic process, avoiding the collision of Majorana zero modes during the braiding. However, in a one-dimensional system, Majorana zero modes cannot bypass each other for braiding. Fortunately, several systems have been proposed to avoid blending Majorana zero modes [25–30]. A well-known approach is to adopt T junctions and manipulate the chemical potential of quantum wires to realize the real-space braiding [25]. In addition, Karzig *et al.* have regulated the direction of the coupling vector to achieve real-space braiding in the traditional Y-junction braiding platform [26]. However, these one-dimensional systems are difficult to be constructed and manipulated, and adiabatic evolution is extremely challenging in experiments.

The emergence of a pair of Majorana corner states provides a new platform for braiding in a second-order topological superconductor, where the Majorana corner states can be manipulated via in-plane magnetic field and proximity-induced spin-singlet superconductivity [31]. Correspondingly, the adiabatical braiding of zero-dimensional Majorana corner states can be realized without the collision of two Majorana corner states. In Ref. [32], a minimal model for second-order topological superconductors is constructed to achieve the braiding by tuning the direction of the in-plane magnetic field. During the braiding process, the external magnetic field is necessary. Due to the Meissner effect, the magnetic field is not allowed to exist within a superconductor. The braiding of non-Abelian anyons also exists in nonsuperconducting systems [33–35]. It is also useful to study how to overcome Meissner effect to achieve braiding in superconducting systems. In graphene, it is known that the edge magnetism arises in the zigzag nanoribbons [36–39] and is sufficiently large enough to open up the edge gap to host the higher-order topological phase [40].

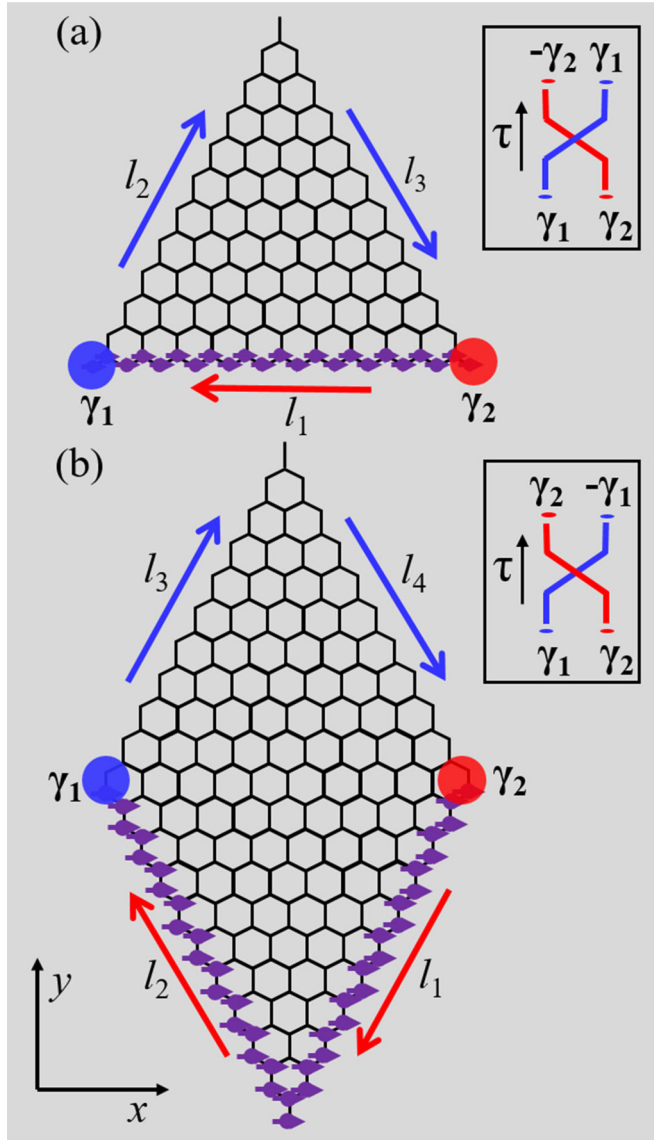*zhangyt@mail.hebtu.edu.cn

†qiao@ustc.edu.cn

FIG. 1. Schematic of Kane-Mele-type nanoflakes on top of an *s*-wave superconductor (gray region). (a), (b) Triangular and diamond-shaped nanoflakes. Inset: The world lines of the two Majorana corner states in the space-time $(x; \tau)$ diagram. The *x*-direction boundary ferromagnetism is represented by the purple arrow on the sublattices. The blue (red) arrows represent the γ_1 (γ_2) moving path during the braiding process.

Inspired by these unique physical properties, we propose to design and study the second-order topological superconductor by using the Kane-Mele-type triangular-shaped nanoflake on top of a superconducting substrate (gray region), as displayed in Fig. 1(a). Due to the parity superconductivity criterion [41,42], time-reversal invariant topological insulators naturally open superconducting gaps and become topological trivial superconductors. Further application of boundary ferromagnetism l_1 (purple arrow) breaks the time-reversal symmetry. Consequently, the system is driven into a second-order topological superconductor. Majorana corner states appear at γ_1 (blue) and γ_2 (red). By manipulating the strengths of magnetization along three different boundaries

(i.e., l_1, l_2, and l_3), one can see that γ_1 (γ_2) moves along the blue (red) arrows along the triangle-shaped boundaries. Since γ_1 crosses the phase-cut line of γ_2, $\gamma_1 \longrightarrow -\gamma_2$, and $\gamma_2 \longrightarrow \gamma_1$, as displayed in Fig. 1(a), the two Majorana zero modes γ_1 and γ_2 make a non-Abelian braiding process in the path successively. Importantly, the Majorana corner states are adiabatically moved at the boundaries without collision during the braiding process. We also study a diamond-shaped nanoflake system, which hosts the two Majorana corner states in diagonal positions as displayed in Fig. 1(b). By manipulating the strengths of boundary magnetization, γ_1 and γ_2 swap respectively along the blue and red arrows, realizing the topological braiding.

The remainder of the paper is organized as follows. In Sec. II, we introduce the tight-binding Hamiltonian of the Kane-Mele model with boundary magnetism on top of an *s*-wave superconductor. In Sec. III A, we plot the energy spectra of the zigzag nanoribbon with boundary magnetism on top of an *s*-wave superconductor and demonstrate the second-order topological phase transition process. Then in Secs. III B and III C, we investigate the distribution and braiding of the Majorana corner states in both triangular and diamond-shaped nanoflakes. A brief summary is presented in Sec. IV.

II. MODEL AND HAMILTONIAN

The corresponding tight-binding model Hamiltonian of the honeycomb lattice can be written as [43]

$$H = -t \sum_{\langle i,j \rangle, \sigma} c_{i\sigma}^{\dagger} c_{j\sigma} + \sum_{\langle\langle i,j \rangle\rangle, \sigma, \sigma'} i\lambda \nu_{ij} c_{i\sigma}^{\dagger} [\hat{\mathbf{s}}_z]_{\sigma\sigma'} c_{j\sigma'}$$
$$+ \sum_{l, \sigma, \sigma'} B_l c_{l\sigma}^{\dagger} [\hat{\mathbf{m}} \cdot \hat{\mathbf{s}}_x]_{\sigma\sigma'} c_{l\sigma'} + \text{H.c.}, \quad (1)$$

where $c_{i\sigma} (c_{i\sigma}^{\dagger})$ is the annihilation (creation) operator for an electron at site i with σ spin. t is the hopping amplitude between nearest neighboring sites. The second term is the intrinsic spin-orbit coupling between next nearest neighbors, with λ measuring the coupling strength. $\nu_{ij} = \pm 1$ indicate counterclockwise and clockwise hopping paths from site j to i, respectively. The third term represents the magnetism of the three boundaries l_1, l_2, and l_3 in Fig. 1(a). The magnetization B_1, B_2, and B_3 can be mediated by the ferromagnetic gates at the graphene nanoflake boundaries [44,45]. For a diamond-shaped nanoflake, the magnetic intensities of the four boundaries l_1, l_2, l_3, and l_4 are respectively set to be B_1, B_2, B_3, and B_4, as displayed in Fig. 1(b). The magnetic orientation is along the unit vector $\hat{\mathbf{m}} = (1, 0)$, meaning that the direction of magnetization is always along the *x* direction. $\hat{\mathbf{s}}_{x,y,z}$ are Pauli matrices.

The superconducting proximity effect between a superconductor and graphene nanoflake induces a finite pairing potential Δ. Thus, the system should be described by a Bogoliubov–de Gennes Hamiltonian in the 4×4 spin $\bigotimes$ Nambu space:

$$\mathbf{H}_{\text{BdG}} = \begin{pmatrix} H & i\Delta\hat{\mathbf{s}}_y \\ -i\Delta^*\hat{\mathbf{s}}_y & -H^* \end{pmatrix}, \quad (2)$$

where the basis vector is $[c_{i\uparrow}, c_{i\downarrow}, c_{i\uparrow}^{\dagger}, c_{i\downarrow}^{\dagger}]^T$.
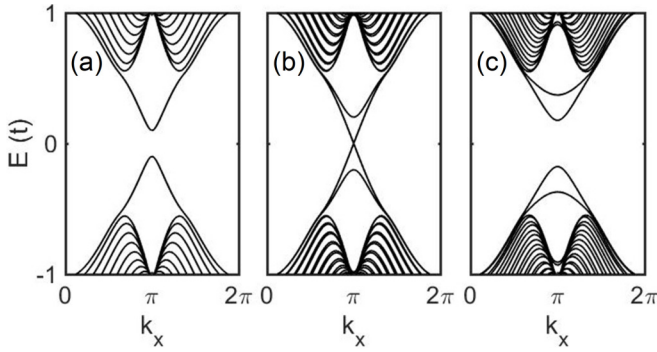
FIG. 2. Energy spectra for the zigzag nanoribbon on top of an s-wave superconductor with different edge magnetization strengths (a) $B_l = 0$, (b) $B_l = 0.1t$, and (c) $B_l = 0.3t$. Other parameters are set to be $t = 1$, $\lambda = 0.1t$, and $\Delta = 0.1t$.

III. RESULTS AND DISCUSSION

A. Zigzag edge states analysis

To illustrate the relationship between s-wave superconductivity and edge magnetism in the second-order topological phases, we plot the energy spectra for the zigzag nanoribbon on top of an s-wave superconductor with different edge magnetization strengths B_l in Fig. 2. Other parameters are set to be $t = 1$, $\lambda = 0.1t$, and $\Delta = 0.1t$, and the nanoribbon width is chosen to be $N = 40a$. At $B_l = 0$, due to the s-wave superconducting proximity effect, a superconducting gap of 2Δ in Fig. 2(a) opens. By introducing magnetization along the zigzag boundary, the energy gap of edge states is completely closed at $B_l = \Delta = 0.1t$ as shown in Fig. 2(b). The gap reopens with further increase of the edge magnetization strength [see Fig. 2(c) with $B_l = 0.3t$]. Both the magnetization and superconductor can introduce a gap in the helical edge, but arising from completely different physical mechanisms. The system forms a domain wall between the $|B_l| > |\Delta|$ boundary and $|B_l| < |\Delta|$ boundary, which gives rise to a Majorana bound state. The magnetization flips the spin of an incoming electron (hole), while the superconductor turns an incoming electron with spin up into an outgoing hole with spin down. These two different types of reflection processes combine together to form a Majorana bound state.

B. Triangular-shaped model

Let us start our discussion with a study of an equilateral triangle-shaped nanoflake with the length of boundary $L_n = 60a$, with a being the lattice constant. Other parameters are set to be $\lambda = 0.1t$, $\Delta = 0.1t$, $B_1 = 0.3t$, and $B_2 = B_3 = 0$. In Fig. 3, we calculate the energy spectra of the triangular-shaped nanoflake deposited on a superconducting substrate. One can see the in-gap zero-energy Majorana corner states (in blue) with a neutral charge, the wave-function distributions of which (blue density dots) are highlighted in the inset of Fig. 3. The Majorana corner states are only sightly extended along the edges l_2 and l_3. The reason is that the energy gap of edge l_1 is greater than the superconducting gap of edges l_2 and l_3, as shown in Figs. 2(a) and 2(c). When the energy gap is large, the barrier is larger. Then the expansion is difficult. Slight expansion does not affect the formation of the Majorana corner
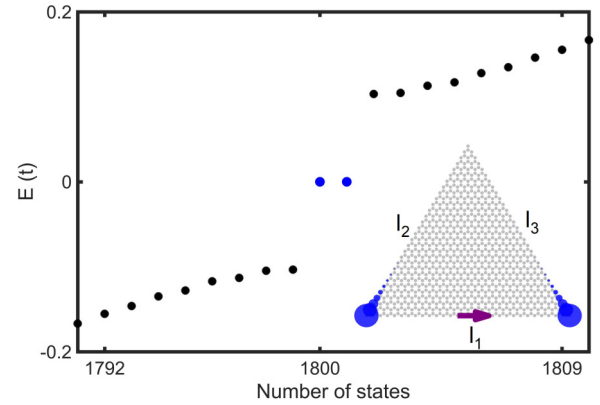

FIG. 3. Energy levels of a finite-sized triangular-shaped Kane-Mele-type nanoflake on top of an s-wave superconductor. The blue dots represent the in-gap Majorana corner states. The wave-function distribution (blue density dots) of the corner states is plotted in the inset. The purple arrow indicates the magnetized boundary. The equilateral triangle-shaped nanoflake has a length of boundary $L_n = 60a$. The parameters are set to $t = 1$, $\lambda = 0.1t$, $\Delta = 0.1t$, $B_1 = 0.3t$, and $B_2 = B_3 = 0$.

states. This clearly indicates that the second-order topological superconductor is produced due to the time-reversal breaking by applying the system boundary magnetism.

When the Majorana corner states appear in pairs at the same position, the interpretation of non-Abelian exchange statistics requires additional symmetry protection [46]. Owing to the magnetized boundary at the l_1 boundary (purple arrow), two isolated Majorana corner states appear at the two corners. In this case, no additional symmetry is needed to protect the isolated Majorana corner states [20]. Thus, the boundary-magnetism induced second-order topological superconductors with Majorana corner states may potentially provide a powerful platform for the appealing topological braiding processing.

To implement topological braiding, we tune the time-dependent intensities of boundary magnetism B_1, B_2, B_3, as displayed in Fig. 4(a). When $|B_l| < |\Delta|$, Majorana bound states cannot exist. When $|B_l| = |\Delta|$, the Majorana bound state expands along the boundary, because of the emergence of the gapless edge states in Fig. 2(b). Remarkably, two Majorana bound states always exist during braiding, even when certain edges become gapless [18]. When $|B_l| > |\Delta|$, Majorana corner states appear. The braiding protocol takes five steps in $T/2$ time to spatially swap γ_1 and γ_2.

(i) At $\tau = 0$, we set $B_1 = 0.3t$, and $B_2 = B_3 = 0$. One can see that two Majorana corner states γ_1 and γ_2 arise respectively at the left and right corners [see Fig. 4(b)]. These two states can be considered as our initial state in the topological braiding processing.

(ii) For $\tau \in (0, T/6)$, B_1 decreases from $0.3t$ to $0.15t$, but B_2 increases from 0 to $0.15t$. As displayed in Fig. 4(c), γ_2 is located still at the right corner, but γ_1 moves from the left to the upper corner along the l_2 boundary (blue arrow).

(iii) For $\tau \in (T/6, T/3)$, B_1 gradually decreases to zero and B_2 increases to $0.3t$. As displayed in Fig. 4(d), γ_1 is located still at the upper corner, but γ_2 moves from the right to the left corner along the l_1 boundary (blue arrow).
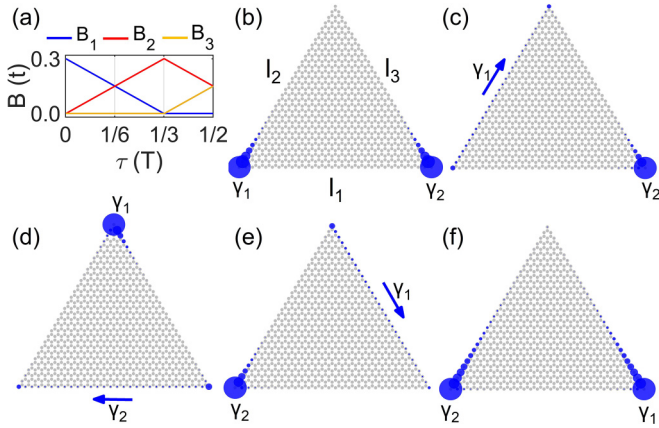
FIG. 4. Exchange of two Majorana corner states by regulating the intensity of magnetization. (a) Time-dependent intensi- ties of boundary magnetism B_1, B_2, B_3 in braiding process. (b)-(f) show the path and the position of the Majorana corner states. The blue density dots indicate zero energy distribu- tion and the blue arrows represent the direction of Majorana corner states movement. The parameters of the initial state are $B_1 = 0.3t$, $B_2 = B_3 = 0$. Other parameters are the same as those in Fig. 3.

(iv) For $\tau \in (T/3, T/2)$, B_2 gradually decreases to $0.15t$ and B_3 increases from 0 to $0.15t$. As displayed in Fig. 4(e), we can see that γ_2 stays still at the left corner, but γ_1 moves from the upper corner to the right corner along the l_3 boundary (blue arrow).

(v) At $\tau = T/2$, the spatial positions of γ_1 and γ_2 are mutually swapped as displayed in Fig. 4(f). The three zigzag boundaries of the triangular-shaped nanoflake are equivalent in the same direction of magnetization and superconductivity. In Fig. 4(f), the domain wall is not formed between the magnetization boundaries l_2 and l_3, and the empty corner between them does not affect the Majorana corner states. When the magnetic field is applied along one edge (l_1) and along the other two edges (l_2 and l_3), the two Majorana corner states appear in the same corners but γ_1 and γ_2 exchange spatial positions, as shown in Figs. 4(a) and 4(f).

Since two Majorana bound states fuse into a Dirac fermion, the simultaneous extension of two Majorana bound states leads to the mixing of Majorana bound states in the triangular-shaped nanoflake. Thus, it is crucial to extend only one Majorana bound state every time to prevent mixing during the braiding process. Interestingly, we can see that γ_1 and γ_2 exchange positions without spatial collision when they move along system boundaries. The braiding operation can be represented by a unitary operator $U(\gamma_1, \gamma_2) = \exp(\frac{\pi}{4}\gamma_1\gamma_2)$. The Majorana corner states can be transformed as $\gamma_1 \longrightarrow -\gamma_2$ and $\gamma_2 \longrightarrow \gamma_1$ [4] [see the inset of Fig. 1(a)].

We present an animation of the period T evolution in the Supplemental Material [47]. For $\tau \in [0, T]$, the spatial positions of γ_1 and γ_2 are swapped twice and the system returns to its initial state. After an exchange process, both Majorana corner states accumulate a π Berry phase and experience a sign flip, with $\gamma_1 \longrightarrow -\gamma_1$ and $\gamma_2 \longrightarrow -\gamma_2$. Moreover, the two Majorana corner states can also be exchanged counter-clockwise by setting the time evolution $\tau \in [T, 0]$.
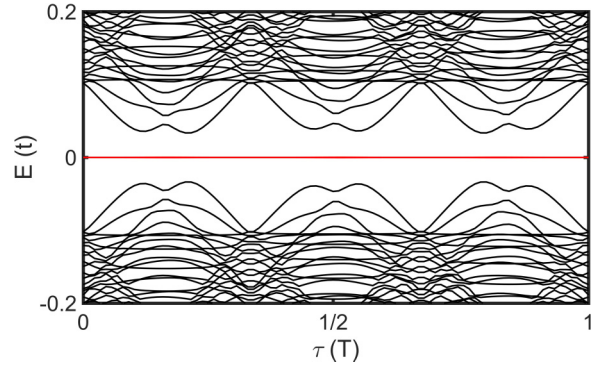

FIG. 5. The energy spectra of the triangular-shaped nanoflake as a function of time τ. The parameter is set to $t = 1, \lambda = 0.1t$, and $\Delta = 0.1t$. Red lines indicate the zero-energy corner states, always separate from the other states (black lines).

To obtain the correct braiding results in the triangular-shaped nanoflake, two Majorana corner states are required to evolve adiabatically during the braiding process. In Fig. 5, we plot the energy spectra of the triangular-shaped nanoflake as a function of time τ, by choosing $\lambda = 0.1t$ and $\Delta = 0.1t$. One can see that the zero-energy states (red line) remain stable throughout the whole process, which indicates that the isolated Majorana corner states can be completely prevented from mixing with other states (black line) by an energy gap. The Majorana extended states locate at the boundary with $|B_l| = |\Delta|$. The Majorana corner states appear at the ends of the boundary with $|B_l| > |\Delta|$. Since the whole system is topologically protected, both the Majorana extended states and Majorana corner states are stable (see Fig. 5). Thus, our results validate the reasonable operation for Majorana corner states.

To verify the robustness of the braiding process, we calculate the exchange of Majorana corner states in a triangular-shaped nanoflake with four different kinds of defects. In Figs. 6(a)–6(c), we consider the case when two atomic sites are missing at the l_1 boundary, as displayed as hollow circles in Fig. 6(a). One can see that two Majorana corner states γ_1 and γ_2 are still located at the two corners, when only the l_1 boundary is magnetized, as displayed in Fig. 6(a). Although the atomic defects exist at the boundary, γ_2 can still move from the right corner to the left corner along the l_1 boundary (blue arrow) in Fig. 6(b). In Figs. 6(d)–6(f), we consider the other case that two atoms are not magnetized, as displayed as red circles in Fig. 6(d). For the initial state of topological braiding processing, two Majorana corner states γ_1 and γ_2 are still located at the two corners of the triangular-shaped nanoflake, as displayed in Fig. 6(d). In Fig. 6(e), γ_2 is shown to move along the magnetic defect boundary. In Figs. 6(g)–6(i), we consider the case when two atomic sites (hollow circles) inside a triangular-shaped nanoflake are missing. The braiding operation relies on boundary effects. Thus, braiding results are insensitive to bulk defects. In Figs. 6(j)–6(l), we consider the case when two atomic sites (hollow circles) at the left corner are missing. It is noted that the braiding results do not change even if the corner lattices are missing. The energy of the in-gap ground states is slightly deviated from zero due to the finite-size effects in Figs. 6(c), 6(f),
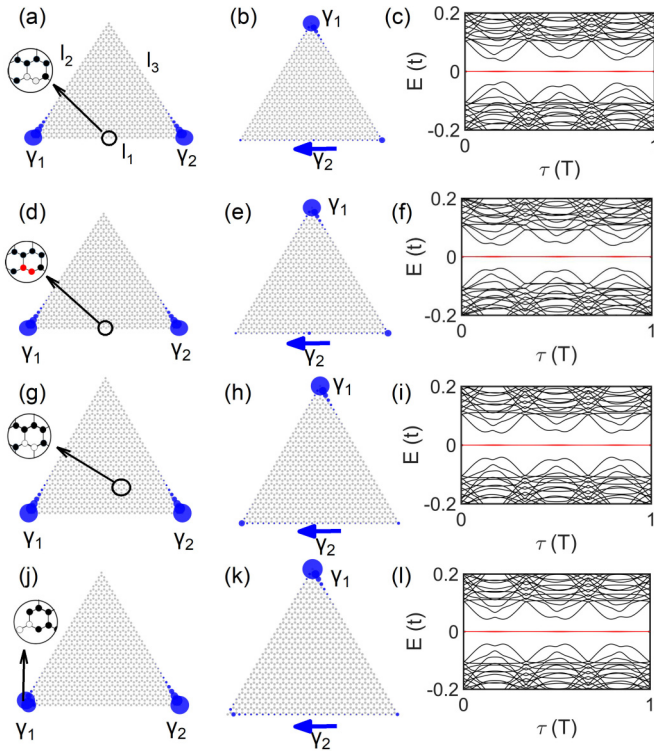
FIG. 6. (a)–(c) Two atomic sites are missing (hollow circles) at the l_1 boundary of a triangular-shaped nanoflake. (d)–(f) Two atoms are not be magnetized (red circles) at the l_1 boundary of a triangular-shaped nanoflake. (g)–(i) Two atomic sites are missing inside a triangular-shaped nanoflake. (j)–(l) Two atomic sites are missing at the left corner of a triangular-shaped nanoflake. (a), (b), (d), (e), (g), (h), (j), (k) The wave-function distributions of two Majorana corner states are shown by blue density dots. (c), (f), (i), (l) The energy spectra as a function of time τ. Red lines indicate the zero-energy corner states, always separate from the other states (black lines). Other parameters are the same as those in Fig. 3.

6(i), and 6(l). The deviation can be eliminated by increasing the size of a nanoflake without changing the physical results. Therefore, the braiding process can still be considered to be adiabatic. Our results show that the exchange of Majorana corner states is robust against the defects. All these suggest that the braiding of Majorana corner states in a triangular-shaped nanoflake can be achieved, even if atomic vacancy defect and magnetic defect appear anywhere. The Majorana bound state is topologically protected, so it is insensitive to small defect perturbations.

To illustrate the degree of robustness to the four different representative kinds of defects, we plotted the energy spectra as a function of defective atom number n, as shown in Fig. 7, with Figs. 6(a), 6(d), 6(g), and 6(j) serving as insets showcasing the location and condition of the defects, respectively. The parameters are set to be $t = 1$, $\lambda = 0.1t$, $\Delta = 0.1t$, $B_1 = 0.15t$, $B_2 = 0.15t$, and $B_3 = 0$, corresponding to the boundary magnetization condition at the maximum zero-energy deviation point in the braiding process in Fig. 6. There is no bulk gap closure and phase transition as the number of missing atoms at the edges increases in Fig. 7(a). Although in-gap states are slightly deviated from zero, this deviation can
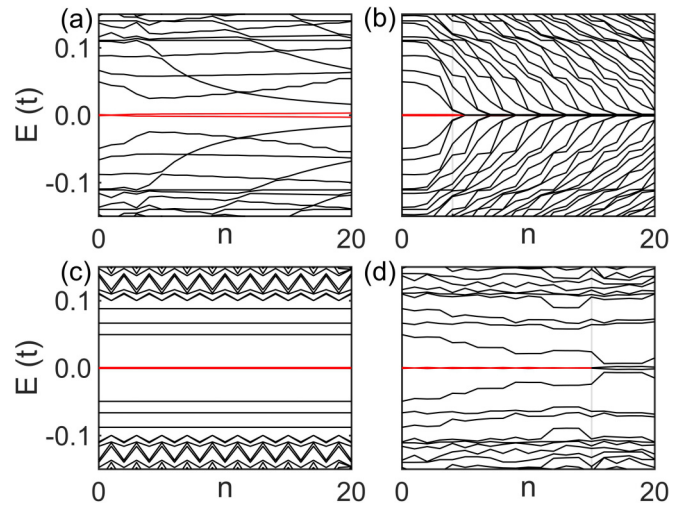

FIG. 7. Energy spectra as a function of the number of atoms with different defects. (a) Atoms are missing at the edge, with Fig. 6(a) as an inset showing the location of the defects. (b) Atoms are nonmagnetized at the edge, with Fig. 6(d) as an inset showing the location of the defects. (c) Atoms are missing inside a triangular-shaped nanoflake, with Fig. 6(g) as an inset showing the location of the defects. (d) Atoms are missing at the corner, with Fig. 6(j) as an inset showing the location of the defects. The parameters are set to $t = 1$, $\lambda = 0.1t$, $\Delta = 0.1t$, $B_1 = 0.15t$, $B_2 = 0.15t$, and $B_3 = 0$.

be eliminated by increasing the size of a nanoflake without changing the physical results. Therefore, it does not destroy the braiding, unless further defects destroy the system structure. For the nonmagnetic atom case as shown in Fig. 7(b), one can see that there are multiple zero-energy states, but the braiding becomes disrupted. The reason is that magnetic defects divide the magnetization boundary into multiple segments, forming multiple edge domain walls. But such case is relatively rare because the boundary magnetism is usually uniformly distributed at zigzag boundaries. For the third kind of defects shown in Fig. 7(c), one can see that the Majorana bound states are not influenced even when 20 atoms are missing inside the triangular-shaped nanoflake. For the fourth case with corner defect, Fig. 7(d) illustrates that the exchange of Majorana corner states is very robust for weak corner defect (smaller n). But there is a significant splitting of the zero-energy state for strong corner defect (larger n), resulting in the disruption of braiding.

C. Diamond-shaped model

Next, we turn to study a diamond-shaped nanoflake with a boundary length of $L_n = 40a$. The parameters are set to be $\lambda = 0.1t$ and $\Delta = 0.1t$. Figure 8(a) displays the energy levels of the diamond-shaped nanoflake deposited on a superconducting substrate, by setting $B_1 = B_2 = 0.3t$ and $B_3 = B_4 = 0$. One can see that the in-gap zero-energy Majorana corner states (blue dots) with a neutral charge appear at the two obtuse angles, as displayed in the inset of Fig. 8(a). The resulting Majorana corner states appear at the opposite corners of the diamond-shaped nanoflake [40,48]. Thus, it is difficult to mix two Majorana corner states in the diamond-shaped nanoflake. Then, we change the parameters to be $B_1 = 0$,
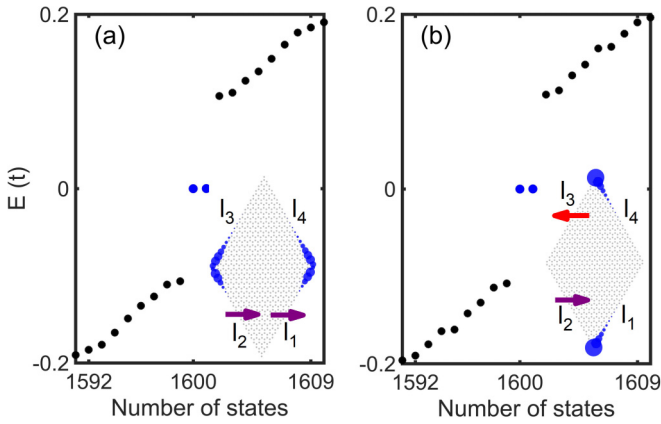
FIG. 8. Energy levels of the finite-sized diamond-shaped Kane-Mele-type nanoflake on top of an s-wave superconductor. The blue dots represent the in-gap corner states. The wave-function distribution (blue density dots) of the corner states is plotted in the inset. (a) The purple arrow indicates the magnetized boundaries l_1 and l_2. The intensities of magnetization are set to $B_1 = B_2 = 0.3t$ and $B_3 = B_4 = 0$. (b) The purple arrow and red arrow indicate the boundaries l_2 and l_3 are magnetized in opposite directions. The diamond-shaped nanoflake has a length of boundary $L_n = 40a$. The parameter is set to $t = 1$, $\lambda = 0.1t$, $\Delta = 0.1t$, $B_1 = 0$, $B_2 = -B_3 = 0.3t$, and $B_4 = 0$.

$B_2 = -B_3 = 0.3t$, and $B_4 = 0$ and calculate the energy level of the diamond-shaped nanoflake, as displayed in Fig. 8(b). One can also see that the in-gap zero-energy Majorana corner states (blue dots) with a neutral charge appear at the two acute angles [see the inset of Fig. 8(b)]. The position of the Majorana corner states can be changed by regulating the strength of boundary magnetism of the diamond-shaped nanoflake. In this way, we can realize the topological quantum braiding via moving of the two Majorana corner states.

Next we focus on the concrete topological quantum braiding process by tuning the time-dependent intensities of boundary magnetism B_1, B_2, B_3, and B_4 as displayed in Fig. 9(a). The braiding protocol takes seven steps to spatially swap γ_1 and γ_2 in $T/2$ time.

(i) At $\tau = 0$, we set $B_1 = B_2 = 0.3t$ and $B_3 = B_4 = 0$. One can see two Majorana corner states γ_1 and γ_2 appear respectively at the left and right obtuse angle, as shown in Fig. 9(b). These two states can be considered as our initial state in topological braiding processing.

(ii) For $\tau \in (0, T/8)$, B_1 decreases from $0.3t$ to $0.15t$, $B_2 = 0.3t$, B_3 decreases from 0 to $-0.15t$, and $B_4 = 0$. As displayed in Fig. 9(c), γ_2 is located still at the right corner, but γ_1 moves from the left to the upper corner along the l_3 boundary (blue arrow).

(iii) For $\tau \in (T/8, T/4)$, B_1 gradually decreases to zero and B_3 decreases to $-0.3t$. As displayed in Fig. 9(d), γ_1 is located still at the upper corner, but γ_2 moves from the right to the bottom corner along the l_1 boundary (blue arrow).

(iv) At $\tau = T/4$, $B_1 = 0$, $B_2 = -B_3 = 0.3t$, and $B_4 = 0$. As displayed in Fig. 9(e), γ_1 and γ_2 go through a clockwise movement to the upper and lower corners.

(v) For $\tau \in (T/4, 3T/8)$, B_2 decreases from $0.3t$ to $0.15t$, and B_4 decreases from 0 to $-0.15t$. As displayed in Fig. 9(f),
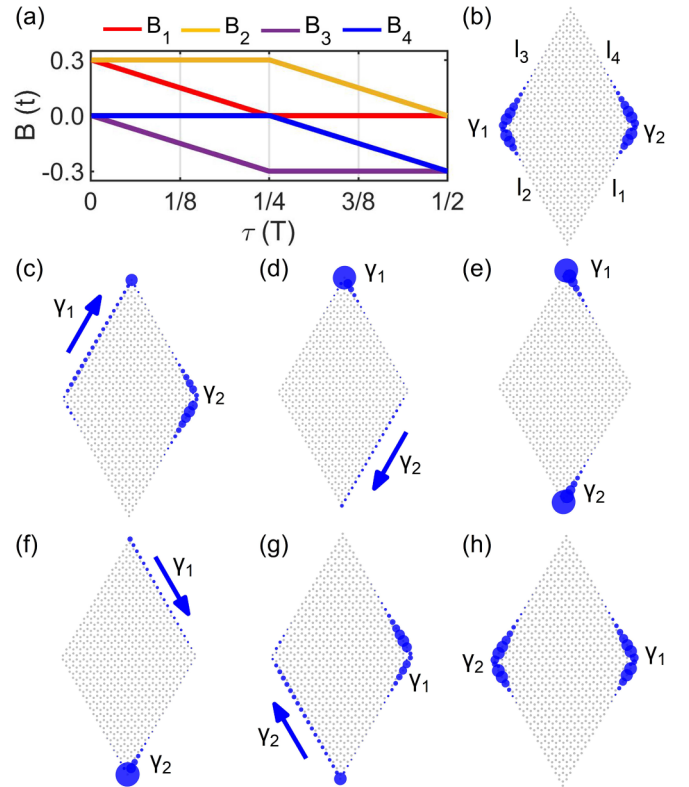

FIG. 9. Exchange of two Majorana corner states by regulating the intensity of magnetization. (a) Time-dependent intensities of boundary magnetism B_1, B_2, B_3, and B_4 in the braiding process. (b)–(h) The path and the position of the Majorana corner states. The blue density dots indicate zero-energy distribution and the blue arrows represent the direction of the Majorana corner states' movement. The parameters of the initial state are $B_1 = B_2 = 0.3t$ and $B_3 = B_4 = 0$. Other parameters are the same as those in Fig. 8.

we can see that γ_2 stays still at the lower corner, but γ_1 moves from the upper corner to the right corner along the l_4 boundary (blue arrow).

(vi) For $\tau \in (3T/8, T/2)$, as B_2 decreases to zero and B_4 decreases to $-0.3t$, γ_1 is located still at the right corner and γ_2 moves from the lower to the left corner along the l_2 boundary (blue arrow), as shown in Fig. 9(g).

(vii) Finally, the spatial positions of γ_1 and γ_2 are swapped at $\tau = T/2$, as shown in Fig. 9(h).

Importantly, we can see that γ_1 and γ_2 exchange positions without spatial collision when they move along the system boundaries. To braid Majorana bound states efficiently, the two Majorana bound states of the diamond-shaped nanoflake can be extended simultaneously along two opposite edges without mixing at $|B_l| = |\Delta|$. The braiding process $\gamma_1 \longrightarrow \gamma_2$ and $\gamma_2 \longrightarrow -\gamma_1$ can be represented by a unitary transformation operation $U(\gamma_2, \gamma_1) = \exp(-\frac{\pi}{4}\gamma_1\gamma_2)$ [4] [see the inset of Fig. 1(b)].

The spatial positions of γ_1 and γ_2 are swapped twice along the diamond-shaped boundaries for $\tau \in [0, T]$, as displayed in the Supplemental Material [47]. The Hamiltonian of the system returns to its initial expression. Such braiding operation can be represented by a unitary operator $U(\gamma_2, \gamma_1) = \exp(-\frac{\pi}{2}\gamma_1\gamma_2)$ with a transformation $\gamma_1 \longrightarrow -\gamma_1$ and $\gamma_2 \longrightarrow$
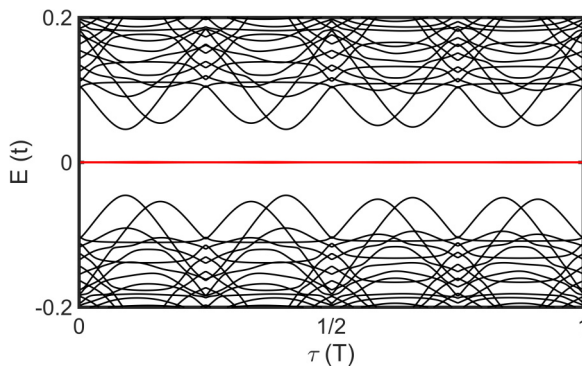
FIG. 10. The energy spectra of the diamond-shaped nanoflake as a function of time τ. The parameter is set to $t = 1, \lambda = 0.1t$, and $\Delta = 0.1t$. Red lines indicate the zero-energy corner states, always separate from the other states (black lines).

$-\gamma_2$. In addition, the two Majorana corner states can also be exchanged counterclockwise by reversing the time evolution to $\tau \in [T, 0]$.

To obtain the correct braiding results in the diamond-shaped nanoflake, two Majorana corner states are required to evolve adiabatically during the braiding process. In Fig. 10, we plot the energy spectra of the diamond-shaped nanoflake as a function of time τ, by choosing $\lambda = 0.1t$ and $\Delta = 0.1t$. One can see that zero-energy states (red line) remain stable throughout the whole process, which indicates that the isolated Majorana corner state can be completely prevented from mixing with other states (black line) by an energy gap. Thus like topological quantum braiding in the triangular-shaped nanoflake in Fig. 4, the operation of Majorana corner states is also controllable and reliable in the diamond-shaped nanoflake. Similar to the braiding process in the triangular-shaped nanoflake, the braiding of Majorana corner states in the diamond-shaped nanoflake is robust against atomic vacancy defect and magnetic defect.

IV. SUMMARY

We have studied Kane-Mele-type topological insulator nanoflakes on top of an s-wave superconductor. The energy levels and the wave-function distributions have been calculated. It is found that two isolated Majorana corner states appear at the corners of the system. It implies that the second-order topological superconductor is induced by the time-reversal symmetry-breaking boundary magnetism. By tuning the time-dependent intensities of boundary magnetism, the Majorana corner states can be transformed as $\gamma_1 \longrightarrow -\gamma_1$ and $\gamma_2 \longrightarrow -\gamma_2$. In addition, we calculated the energy levels and the wave-function distributions of the diamond-shaped nanoflake. Our results show that two Majorana corner states appear at opposite corners of the diamond-shaped nanoflake. We have tuned the boundary magnetization to complete the exchange of γ_1 and γ_2 in the braiding protocol. Importantly, Majorana corner states remain stable throughout the braiding process, which indicates that the isolated Majorana corner state can be completely prevented from mixing with other states by an energy gap. These braiding processes are robust against the atomic vacancy defect and magnetic defect at the boundary. Our proposals will simplify the experimental braiding setup required on the second-order topological superconductor platforms.

[1] A. Kitaev, Anyons in an exactly solved model and beyond, Ann. Phys. (NY) **321**, 2 (2006).

[2] C. Nayak, S. H. Simon, A. Stern, M. Freedman, and S. D. Sarma, Non-Abelian anyons and topological quantum computation, Rev. Mod. Phys. **80**, 1083 (2008).

[3] E. Majorana, Symmetrical theory of electrons and positrons, Nuovo Cimento **14**, 171 (1937).

[4] D. A. Ivanov, Non-Abelian statistics of half-quantum vortices in p-wave superconductors, Phys. Rev. Lett. **86**, 268 (2001).

[5] A. Y. Kitaev, Unpaired Majorana fermions in quantum wires, Phys. Usp. **44**, 131 (2001).

[6] S. Ran, C. Eckberg, Q.-P. Ding, Y. Furukawa, T. Metz, S. R. Saha, I.-L. Liu, M. Zic, H. Kim, J. Paglione, and N. P. Butch, Nearly ferromagnetic spin-triplet superconductivity, Science **365**, 684 (2019).

[7] L. Jiao, S. Howard, S. Ran, Z. Wang, J. O. Rodriguez, M. Sigrist, Z. Wang, N. P. Butch, and V. Madhavan, Chiral superconductivity in heavy-fermion metal UTe$_2$, Nature (London) **579**, 523 (2020).

[8] V. Mourik, K. Zuo, S. M. Frolov, S. R. Plissard, E. P. A. M. Bakkers, and L. P. Kouwenhoven, Signatures of Majorana fermions in hybrid superconductor-semiconductor nanowire devices, Science **336**, 1003 (2012).

[9] A. Das, Y. Ronen, Y. Most, Y. Oreg, M. Heiblum, and H. Shtrikman, Zero-bias peaks and splitting in an Al-InAs nanowire topological superconductor as a signature of Majorana fermions, Nat. Phys. **8**, 887 (2012).

[10] L. P. Rokhinson, X. Liu, and J. K. Furdyna, The fractional a.c. Josephson effect in a semiconductor-superconductor nanowire as a signature of Majorana particles, Nat. Phys. **8**, 795 (2012).

[11] A. D. K. Finck, D. J. V. Harlingen, P. K. Mohseni, K. Jung, and X. Li, Anomalous modulation of a zero-bias peak in a hybrid nanowire-superconductor device, Phys. Rev. Lett. **110**, 126406 (2013).

[12] H. O. H. Churchill, V. Fatemi, K. Grove-Rasmussen, M. T. Deng, P. Caroff, H. Q. Xu, and C. M. Marcus, Superconductor-nanowire devices from tunneling to the multichannel regime: Zero-bias oscillations and magnetoconductance crossover, Phys. Rev. B **87**, 241401(R) (2013).

[13] M. T. Deng, S. Vaitiekėnas, E. B. Hansen, J. Danon, M. Leijnse, K. Flensberg, J. Nygård, P. Krogstrup, and C. M. Marcus, Majorana bound state in a coupled quantum-dot hybrid-nanowire system, Science **354**, 1557 (2016).

[14] S. Nadj-Perge, I. K. Drozdov, J. Li, H. Chen, S. Jeon, J. Seo, A. H. MacDonald, B. A. Bernevig, and A. Yazdani, Observation of Majorana fermions in ferromagnetic atomic chains on a superconductor, Science **346**, 602 (2014).

[15] N. Read and D. Green, Paired states of fermions in two dimensions with breaking of parity and time-reversal symmetries and the fractional quantum Hall effect, Phys. Rev. B **61**, 10267 (2000).

[16] M. Stone and R. Roy, Edge modes, edge currents, and gauge invariance in $p_x + ip_y$ superfluids and superconductors, Phys. Rev. B **69**, 184511 (2004).

[17] J. Langbehn, Y. Peng, L. Trifunovic, F. von Oppen, and P. W. Brouwer, Reflection-symmetric second-order topological insulators and superconductors, Phys. Rev. Lett. **119**, 246401 (2017).

[18] X. Zhu, Tunable Majorana corner states in a two-dimensional second-order topological superconductor induced by magnetic fields, Phys. Rev. B **97**, 205134 (2018).

[19] T. Liu, J. J. He, and F. Nori, Majorana corner states in a two-dimensional magnetic topological insulator on a high-temperature superconductor, Phys. Rev. B **98**, 245413 (2018).

[20] X.-H. Pan, K.-J. Yang, L. Chen, G. Xu, C.-X. Liu, and X. Liu, Lattice-symmetry-assisted second-order topological superconductors and Majorana patterns, Phys. Rev. Lett. **123**, 156801 (2019).

[21] Z. Yan, Higher-order topological odd-parity superconductors, Phys. Rev. Lett. **123**, 177001 (2019).

[22] Y. Wang, M. Lin, and T. L. Hughes, Weak-pairing higher order topological superconductors, Phys. Rev. B **98**, 165144 (2018).

[23] Z. Wu, Z. Yan, and W. Huang, Higher-order topological superconductivity: Possible realization in Fermi gases and Sr_2RuO_4, Phys. Rev. B **99**, 020508(R) (2019).

[24] X. Zhu, Second-order topological superconductors with mixed pairing, Phys. Rev. Lett. **122**, 236401 (2019).

[25] J. Alicea, Y. Oreg, G. Refael, F. von Oppen, and M. P. A. Fisher, Non-Abelian statistics and topological quantum information processing in 1D wire networks, Nat. Phys. **7**, 412 (2011).

[26] T. Karzig, Y. Oreg, G. Refael, and M. H. Freedman, Universal geometric path to a robust Majorana magic gate, Phys. Rev. X **6**, 031019 (2016).

[27] J. Liu, W. Chen, M. Gong, Y. Wu, and X. Xie, Minimal setup for non-Abelian braiding of Majorana zero modes, Sci. China Phys. Mech. **64**, 117811 (2021).

[28] R. V. Mishmash, B. Bauer, F. von Oppen, and J. Alicea, Dephasing and leakage dynamics of noisy Majorana-based qubits: Topological versus Andreev, Phys. Rev. B **101**, 075404 (2020).

[29] I. C. Fulga, B. van Heck, M. Burrello, and T. Hyart, Effects of disorder on Coulomb-assisted braiding of Majorana zero modes, Phys. Rev. B **88**, 155435 (2013).

[30] J. Manousakis, C. Wille, A. Altland, R. Egger, K. Flensberg, and F. Hassler, Weak measurement protocols for Majorana bound state identification, Phys. Rev. Lett. **124**, 096801 (2020).

[31] T. E. Pahomi, M. Sigrist, and A. A. Soluyanov, Braiding Majorana corner modes in a second-order topological superconductor, Phys. Rev. Res. **2**, 032068(R) (2020).

[32] S.-B. Zhang, W. B. Rui, A. Calzona, S.-J. Choi, A. P. Schnyder, and B. Trauzettel, Topological and holonomic quantum computation based on second-order topological superconductors, Phys. Rev. Res. **2**, 043025 (2020).

[33] Y. Wu, H. Jiang, J. Liu, H. Liu, and X. C. Xie, Non-Abelian braiding of Dirac fermionic modes using topological corner states in higher-order topological insulator, Phys. Rev. Lett. **125**, 036801 (2020).

[34] Y. Wu, H. Jiang, H. Chen, H. Liu, J. Liu, and X. C. Xie, Non-Abelian braiding in spin superconductors utilizing the Aharonov-Casher effect, Phys. Rev. Lett. **128**, 106804 (2022).

[35] Z.-X. Lin, Y. Wu, and X. C. Xie, Non-Abelian operation through scattering between chiral Dirac edge modes, Phys. Rev. B **105**, 205428 (2022).

[36] Y.-W. Son, M. L. Cohen, and S. G. Louie, Energy gaps in graphene nanoribbons, Phys. Rev. Lett. **97**, 216803 (2006).

[37] J. Jung and A. H. MacDonald, Carrier density and magnetism in graphene zigzag nanoribbons, Phys. Rev. B **79**, 235433 (2009).

[38] M. Golor, T. C. Lang, and S. Wessel, Quantum Monte Carlo studies of edge magnetism in chiral graphene nanoribbons, Phys. Rev. B **87**, 155441 (2013).

[39] G. Z. Magda, X. Jin, I. Hagymási, P. Vancsó, Z. Osváth, P. Nemes-Incze, C. Hwang, L. P. Biró, and L. Tapasztó, Room-temperature magnetic order on zigzag edges of narrow graphene nanoribbons, Nature (London) **514**, 608 (2014).

[40] C.-M. Miao, Q.-F. Sun, and Y.-T. Zhang, Second-order topological corner states in zigzag graphene nanoflake with different types of edge magnetic configurations, Phys. Rev. B **106**, 165422 (2022).

[41] L. Fu, and E. Berg, Odd-parity topological superconductors: Theory and application to $Cu_xBi_2Se_3$, Phys. Rev. Lett. **105**, 097001 (2010).

[42] M. Sato, Topological odd-parity superconductors, Phys. Rev. B **81**, 220504(R) (2010).

[43] C. L. Kane and E. J. Mele, $\mathbb{Z}_2$ topological order and the quantum spin Hall effect, Phys. Rev. Lett. **95**, 146802 (2005).

[44] H. X. Yang, A. Hallal, D. Terrade, X. Waintal, S. Roche, and M. Chshiev, Proximity effects induced in graphene by magnetic insulators: First-principles calculations on spin filtering and exchange-splitting gaps, Phys. Rev. Lett. **110**, 046603 (2013).

[45] H. Haugen, D. Huertas-Hernando, and A. Brataas, Spin transport in proximity-induced ferromagnetic graphene, Phys. Rev. B **77**, 115406 (2008).

[46] P. Gao, Y.-P. He, and X.-J. Liu, Symmetry-protected non-Abelian braiding of Majorana Kramers pairs, Phys. Rev. B **94**, 224509 (2016).

[47] See Supplemental Material at http://link.aps.org/supplemental/10.1103/PhysRevB.109.115413 for the animations for braiding Majorana corner states.

[48] Y. Ren, Z. Qiao, and Q. Niu, Engineering corner states from two-dimensional topological insulators, Phys. Rev. Lett. **124**, 166804 (2020).